Ballistic transport in graphene antidot lattices

Ryuta Yagi, Ryoji Sakakibara, Ryoya Ebisuoka, and Jumpei Onishi
Graduate School of Advanced Sciences of Matter (AdSM), Hiroshima University, Higashi-Hiroshima 1-3-1, Hiroshima 739-8530, Japan

Kenji Watanabe and Takashi Taniguchi
National Institute for Material Sciences (NIMS), Namiki 1-1, Tsukuba 305-0044, Japan

Yasuhiro Iye
Institute for Solid State Physics, University of Tokyo, Kashiwanoha 5-1-5, Kashiwa, Chiba 277-8581, Japan
(Received 18 June 2015; revised manuscript received 23 September 2015; published 6 November 2015)

We observed commensurability magnetoresistance arising from ballistic electron transport in a triangular antidot lattice of high-mobility graphene. For both the monolayer and bilayer, magnetoresistance peaks were observed at the commensurability magnetic fields of the cyclotron orbit with an antidot lattice. This condition was approximately unchanged for massless and massive Dirac fermions. The peaks appeared when the carrier mean free path was roughly larger than the lattice constant of the antidot, which indicates that the effect stems from the short-range characteristics of the carrier's scattering with antidots. We also found that the magnitude of the commensurability peak diminished with changing the gate voltages to the charge neutrality point. This arose from the screening of the charged impurity in graphene, which is dependent on the carrier density.

DOI: 10.1103/PhysRevB.92.195406 PACS number(s): 72.80.Vp, 73.23.Ad

I. INTRODUCTION

Graphene has attracted interest in a variety of fields because it is expected to be a promising candidate for next-generation devices [1,2]. It has a number of significant features [1,2] that differ from conventional electron systems, and which have been extensively studied since its discovery [3]. One of its remarkable features is the linear dispersion relation of its electronic band structure. Unlike conventional electron systems, external fields do not change the magnitude of velocity. The other feature is a bipolar property. Also, graphene has a π-Berry phase. It would seem that all these would affect the wave packet dynamics of a carrier in graphene, but this remains unclear. The most logical way to study the wave packet dynamics would be to measure the transport properties in the ballistic regime. Although there have been a number of experimental studies in the diffusive regime, ballistic transport has been less explored. In this paper we investigate one such phenomenon, commensurability magnetoresistance, using the antidot lattices of high-mobility graphene.

An antidot lattice is a two-dimensional conductor with a regular array of holes. In low magnetic fields, the motions of the ballistic electrons are chaotic because cyclotron orbits are interrupted by successive collisions with the antidots. [See Fig. 1(a).] However, at magnetic fields of the commensurate condition, regular orbit connecting antidots appear (orbits 4 and 5) [4–7]. The simplest commensurability condition is for orbit 4, given by

$$2R_c = a, \tag{1}$$

where $R_c = \hbar k_F/eB$ is a cyclotron radius and a is the lattice constant. (k_F is the Fermi wave vector and B is a magnetic field.) This is the condition in which runaway orbits connecting to nearest-neighbor antidots appear. Electrons propagate one dimensionally via successive collisions with antidot lattices, which results in a magnetoresistance peak. There are other regular orbits whose center of gravity is unchanged, but these do not contribute to the commensurability magnetoresistance peaks.

In terms of conventional two-dimensional electron systems, the electronic properties of antidot lattices have been extensively studied both theoretically and experimentally using GaAs/AlGaAs heterostructures since the 1990's [4,8–13]. Commensurability magnetoresistance has been used in studies on composite fermions [14,15], quasiparticle dynamics in the Andreev reflection process [16,17], Hofstadter's butterfly energy diagram [18], and to determine the shape of a Fermi surface [19]. In terms of graphene, there have been a few experiments on antidot lattices in diffusive regimes [20–22].

II. EXPERIMENT

To observe ballistic electron transport, the mean free path of a carrier should be larger than the typical structure of the device. The experiments performed in the present study were done using triangular antidot lattices made of high-mobility graphene. We fabricated graphene used in this study by mechanically exfoliating high-quality Kish graphite. Graphene was transferred directly on a SiO_2/Si substrate or on a thin h-BN flake that was mechanically exfoliated on a SiO_2/Si substrate. The antidot structure was formed by electron beam lithography and oxygen plasma etching. Electric leads were connected to graphene to perform four-probe measurements. The Si substrate was conducting and served as a back gate to change the carrier density. Resistance measurements were done with a standard lock-in technique. The typical excitation current was 100 nA. A magnetic field was applied with a superconducting solenoid. Figure 1(b) shows the optical micrograph of a graphene antidot device on h-BN. The values of carrier mobility for devices without an antidot lattice structure were about 3×10^4 cm^2/V s and 1.5×10^4 cm^2/V s for graphene on h-BN flakes and on SiO_2 substrates, respectively. (See the Appendix.) The mean free paths l_F at the high carrier density (n) regime were larger

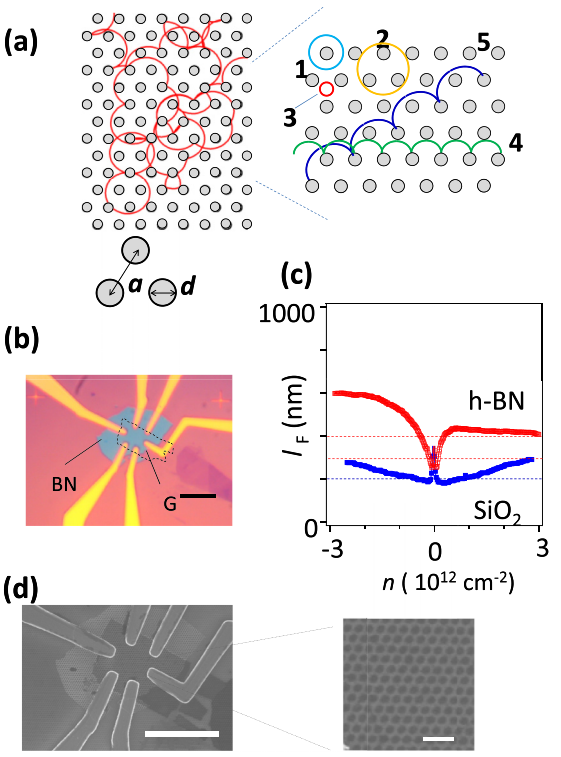

FIG. 1. (Color online) (a) Schematic views of triangular antidot lattice and electron orbits in a magnetic field. a is the distance between the centers of the neighboring antidots and d is the diameter of an antidot. Generally, electron orbits are chaotic in low magnetic fields. Left: However, regular orbits exist under particular conditions. Right: Orbits 1 and 2 enclose one and three antidot(s), respectively. Orbit 3 does not enclose any antidot. The centers of gravity are fixed for these orbits. Orbits 4 and 5 are runaway orbits. (b) Optical micrograph of a graphene device on an h-BN flake. A bar is 10 μm. (c) Carrier density n dependence of mean free path l_F of two-dimensional graphene, i.e., without antidot structures. Dashed lines indicate some of the values of a for comparison with l_F. Carriers are electrons for $n > 0$ and holes for $n < 0$. (d) SEM micrograph of graphene antidot device on BN. Right: A bar is 10 μm. Left: A bar is 1000 nm.

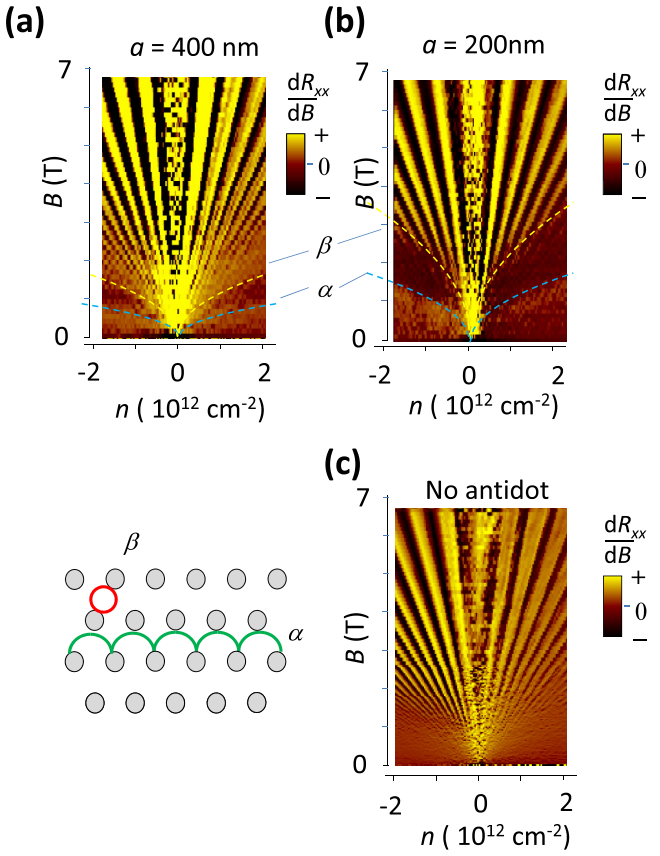

FIG. 2. (Color online) Commensurability magnetoresistance of monolayer graphene antidot lattice. (a) A color scale mapping of dR_{xx}/dB for a graphene antidot sample with $a = 400$ nm made on an h-BN flake. R_{xx} is the diagonal resistance, and B is the magnetic field. a is an antidot lattice constant. n is the carrier density. Carriers are electrons for $n > 0$ and holes for $n < 0$. Dashed lines denoted by α are commensurability magnetoresistance peaks, $2R_c = a$. Dashed lines β are for a condition $2R_c = (a - d)$, i.e., the cyclotron diameter equals the minimum conducting channel width $(a - d)$. The illustration shows typical carrier orbits under these conditions. (b) A mapping for a graphene antidot sample with $a = 200$ nm made on a SiO_2 substrate. (c) A mapping for a 2D graphene sample (without an antidot structure).

than the antidot lattice periods. As shown in Fig. 1(c), l_F reached about 600 nm (for antidot lattice samples with $a = 400$ and 300 nm) and 250 nm (for $a = 200$ nm). The values of a in the actual device and the diameter d of the antidots were determined by a scanning electron microscopy (SEM) micrograph [Fig. 1(d)].

III. RESULT AND DISCUSSION

Characteristic magnetoresistance arising from the antidot lattice structure was observed in the low magnetic field regime. Figure 2(a) shows a color scale mapping of dR_{xx}/dB as a function of carrier density n and magnetic field B for an antidot sample with $a = 400$ nm ($d = 180$ nm). Here, R_{xx} is a diagonal resistance. Fan-shaped stripes in high magnetic fields are peaks due to the Shubnikov–de Haas (SdH) effect. The antidot sample was verified to be a monolayer because all the Landau levels, including the zero mode appearing at the charge neutrality point, had the same degeneracy [3]. In the low magnetic field regime, we could discern broad magnetoresistance peaks (dashed line α) originating from the antidot structure. The peak positions shifted to higher magnetic fields for smaller antidot period samples, as seen in the results [Fig. 2(b)] for antidots with a half lattice constant ($a = 200$ nm, $d = 100$ nm). In samples without antidots, no such peaks were visible in the low magnetic field regime [Fig. 2(c)]. The observed V_g dependence of the peak magnetic fields B_p could be explained by commensurability magnetoresistance. The dashed lines α are theoretical values of B_p for the basic commensurability condition

$$B_p = (2\hbar/ea)\sqrt{\pi|n|}, \tag{2}$$

which was yielded from Eq. (1). Here, $n = C_g(V_g - V_0)/e$, V_0 is the gate voltage of the charge neutrality point, and C_g is a gate capacitance.

The peak structure is clearly visible in traces of the magnetic field sweep, as shown in Fig. 3(a). The red arrows are peak

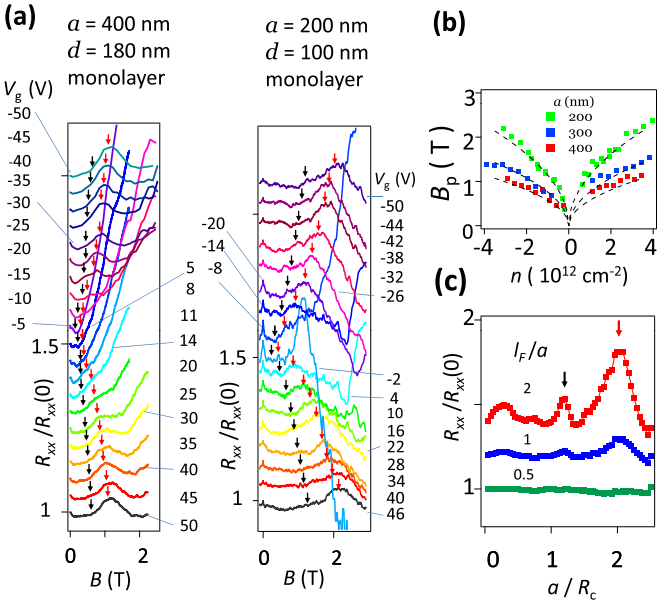

FIG. 3. (Color online) Analysis of commensurability peak positions. (a) B dependence of normalized diagonal resistivity $R_{xx}/R_{xx}(0)$ for different gate voltages. V_g is the gate voltage. B is the magnetic field. R_{xx} is the diagonal resistance. $R_{xx}(0)$ is for zero magnetic field. Data are for a monolayer graphene antidot device with $a = 400$ nm (left) and 200 nm (right). Data for different V_g's are offset. Red arrows are commensurability peak positions for the nearest-neighbor antidots. Black arrows are commensurability peak positions for the next-nearest-neighbor antidots. (b) Dependence of peak magnetic field B_p on carrier density n. Dashed lines are B_p calculated using the commensurability condition. (c) Numerical simulation of diagonal magnetoresistance. R_{xx} is the diagonal resistance. $R_{xx}(0)$ is R_{xx} at zero magnetic field. Data were offset. R_c is the cyclotron radius. a is an antidot lattice constant. l_F is the mean free path. Arrows at $a/R_c \approx 2$ and 1.2 indicate commensurability conditions for the nearest-neighbor and the next-nearest-neighbor antidots, respectively.

positions calculated with Eq. (2). With increasing V_g from $V_g = -50$ V (top), the peak magnetic fields shifted to the lower magnetic fields, and near the charge neutrality point ($V_g \sim 0$ V), they turned and started shifting to the higher magnetic fields. Large peaks visible near the neutrality point are due to Landau levels with index $N = 0$ or ± 1.

To investigate the details of the commensurability condition, we plotted the n dependence of the peak magnetic fields in Fig. 3(b) for antidot devices with different values of a, together with peak positions calculated with $2R_c = a$. The peak magnetic field had a square-root dependence of the carrier density as in Eq. (2). This is fundamentally different from the behavior of the SdH oscillation peaks. They have a linear dependence on n because the degeneracy of the Landau level is proportional to the magnetic field. Peaks for samples with smaller values of a appear in higher magnetic fields because B_p is inversely proportional to the lattice constant, as expected from Eq. (2).

Generally, ballistic transport requires a sufficiently long mean free path l_F. An issue that needs to be considered is how long the l_F should be for observing commensurability peaks. Figure 3(c) shows the numerically calculated magnetoresistance of Dirac electrons for a triangular antidot lattice using a Kubo-type formula [5],

$$\sigma_{ij} = A \int_0^\infty \langle v_i(t) \cdot v_j(0) \rangle \exp(-t/\tau) dt, \qquad (3)$$

where A is a constant, σ_{ij} is a conductivity, v_i and v_j are the i and j components of velocity, and $\langle \cdots \rangle$ is the average over phase space. Conductivity components σ_{xx} and σ_{xy} were calculated using Eq. (2), and ρ_{xx} was obtained by tensor inversion. The parameter for this simulation is $d/a = 0.4$, which is close to that of the experiment. The orbits and velocities were calculated semiclassically. It was assumed that there is no potential variation in the conducting channel, that a carrier orbit consists of a circle or arcs of circles, and that specular scattering occurs at the boundary of the antidots. A peak structure was clearly visible around $a/R_c = 2$, which is equivalent to the basic commensurability condition. (Note that a/R_c is proportional to the magnetic field.) The peak survived at $l_F \sim a$, which could be realized in the present experiment. Qualitative agreement between the theory and the experiment ensured that the peak structures in the magnetoresistance were due to commensurability magnetoresistance. The fact that a basic commensurability magnetoresistance peak was observable in magnetic fields as low as $l_F = a$ indicates that it does not necessarily require a long runaway orbit, but rather occurred from short-range scattering characteristics, as pointed out by Ishizaka and Ando for conventional two-dimensional electron gas (2DEG) [7]. Skipping orbits connecting the nearest-neighbor antidots have an important contribution to the commensurability peak.

Commensurability magnetoresistance was also observed in bilayer graphene. The left panel in Fig. 4(a) shows the results in a bilayer antidot sample with $a = 400$ nm ($d = 180$ nm). The results in monolayer graphene with the same value of a are shown in the right panel, for comparison. In the low magnetic field, a broad peak structure due to the antidot structure was also observed in the bilayer, as indicated by the dashed lines in Fig. 4(a). The peaks satisfied the basic commensurability conditions, as in the monolayer case. In high magnetic fields, SdH oscillation showed a zero energy Landau level with double the degeneracy of the monolayer graphene. Figure 4(b) shows traces of magnetoresistance for $n = 3.3 \times 10^{12}$ cm^{-2}. The magnetic field for commensurability is approximately the same, but the SdH peaks at the same value of n are inverted between the monolayer and bilayer. Results of B_p for other n are plotted in Fig. 4(c). Commensurability magnetoresistance peaks could be described by Eq. (1) for both monolayer and bilayer graphene.

So far, we have seen the peaks for the basic commensurability condition. It is also possible for commensurability with the next-nearest antidots [orbit 5 in Fig. 1(a)]. The commensurability condition is then

$$2R_c = \sqrt{3}a. \qquad (4)$$

Peaks for this condition correspond to small peaks at $a/R_c = 2/\sqrt{3} \approx 1.2$ in the simulation [Fig. 3(c)]. In Fig. 3(a), calculated magnetic fields for this commensurability condition are indicated by black arrows. Near these magnetic fields, hump structures or the indications are visible, though weak, at

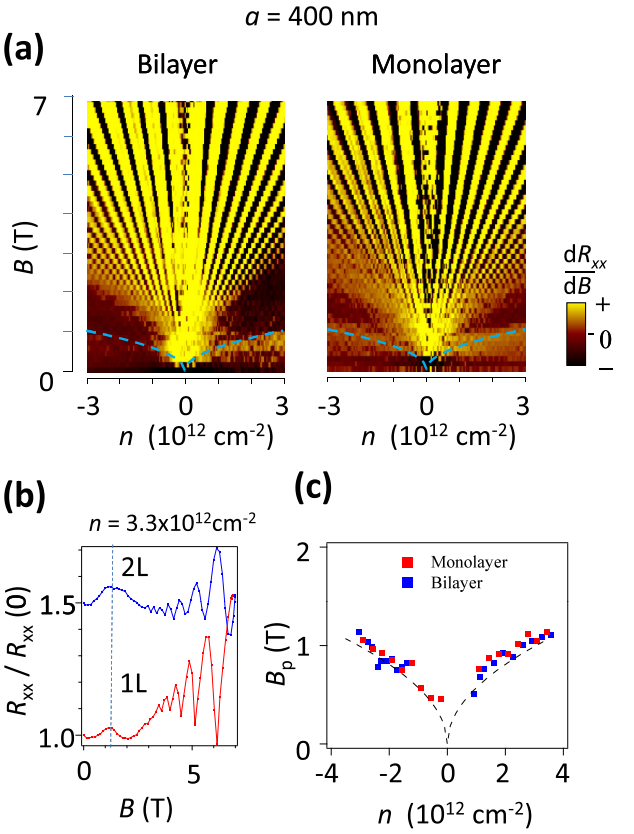

FIG. 4. (Color online) Commensurability peaks for bilayer graphene antidots. (a) Color scale mapping of dR_{xx}/dB for graphene antidots with $a = 400$ nm made on h-BN flakes. R_{xx} is the diagonal resistance. B is the magnetic field. n is the carrier density. a is the antidot lattice constant. The left panel is for bilayer graphene. The right panel is monolayer graphene. The dashed line is the calculated commensurability peak position. (b) B dependence of resistance for monolayer and bilayer antidot samples. Values of the carrier density n were 3.3×10^{12} cm^{-2}. $R_{xx}(0)$ is the diagonal resistance at zero magnetic field. Data for $2L$ are shifted by 0.5. (c) Dependence of B_p on the carrier density. B_p is the magnetic field of a commensurability peak. Red points are for monolayers and blue points are for bilayers. Dashed lines are theory.

some gate bias voltages. Those peaks are also much smaller in magnitude than the basic peak as in the simulation because the carriers travel a longer distance before colliding with the next antidot. To observe large peaks, samples with a larger l_F are required, which can be attained by reducing impurity scattering. The magnitude of the commensurability magnetoresistance peaks is not only determined by a mean free path but also by the aspect ratio that determines the width of the conducting channel. It becomes increasingly difficult to satisfy the commensurability condition for larger cyclotron diameters because of geometrical restrictions. It would be possible that the quality of graphene became a bit, but not significantly, lower than that of a two-dimensional one because of the additional fabrication process to drill the antidots. However, by comparing the calculation with the experiment, l_F was close to 1 because of the presence of the main commensurability peaks.

As shown in Fig. 3(a), the magnitude of the commensurability magnetoresistance diminished as V_g approached the charge neutrality point, i.e., $V_g \sim 0$ V, and it is hardly visible around its vicinity. This can be understood by the variation of l_F with carrier density: l_F decreased with decreasing $|n|$, as shown in Fig. 1(c). This resulted from screening of the impurity potential, that becomes less effective in the low carrier density regime [23]. The mean free path is expected to decrease as $\propto\sqrt{n}$, which is in good qualitative agreement with the experimental results, especially for the higher-mobility samples.

The origin of the observed peak differs from the boundary scattering resistance in one-dimensional wire or thin films [24–26]. The boundary scattering that intervenes with cyclotron motion leads to a magnetoresistance peak. The peak appears when the wire width or thickness of the film w satisfies a condition $2R_c = 2w/0.55$. If an antidot lattice is regarded as a network of wires, the minimum width of the conducting channel is $(a - d)$. The peak magnetic fields for boundary resistance were estimated to occur at $2R_c = 950$ and 510 nm for monolayer antidot samples with $a = 400$ and 200 nm, respectively. The corresponding peak magnetic fields are smaller by factors of about 0.39 and 0.42 than the values for the commensurability peak position.

One other type of commensurability effect is relevant to the cyclotron radius and antidot geometry: threshold magnetic fields for observing the SdH effect. Plotted with dashed lines β in Figs. 2(a) and 2(b) are the threshold magnetic fields for observing the SdH effect, which were calculated with $2R_c = (a - d)$. This is a condition in which a cyclotron diameter equals the minimum conducting channel width. In low magnetic fields, the SdH effect is suppressed because every cyclotron motion is interrupted by collisions with antidots. Complete cyclotron motion becomes possible in larger magnetic fields [orbits 1 and 2 in Fig. 1(a)], but the phase volumes for these orbits are still small because chaotic orbits are dominant. For larger magnetic fields where the cyclotron diameter becomes close to or smaller than $(a - d)$, the phase volume is dominated by fixed orbits [orbit 3 in Fig. 1(a)], and the SdH effect becomes distinct. For this condition, although there are orbits that collide with the antidots, the phase volume for those states diminishes rapidly with increasing magnetic fields. The threshold is irrelevant to the poor mobility of graphene because a SdH effect as low as $B = 1$ T was observed in the samples with no antidot lattice.

IV. SUMMARY

Magnetotransport of a graphene antidot lattice was studied using high-mobility graphene. For both monolayer and bilayer graphene, we observed commensurability magnetoresistance peaks. The magnetic fields of the peaks were approximately the same in monolayer and bilayer graphene. The basic commensurability peaks occurred when the distance between the nearest antidots equaled the cyclotron diameter. A numerical simulation based on the Kubo-type formula qualitatively reproduced the magnetoresistance traces observed in the experiment. The fact that the commensurability peak appears when l_F is larger than about a indicates that short-range scattering characteristics are an important mechanism in the commensurability magnetoresistance.

ACKNOWLEDGMENTS

This work was supported by MEXT KAKENHI Grant No. 25107003. The authors thank T. Ando at the Tokyo Institute of Technology, T. Nakanishi at National Institute of Advanced Industrial Science and Technology (AIST), Japan, and T. Osada at Institute for Solid State Physics (ISSP), the University of Tokyo, for fruitful discussions

APPENDIX: BASIC CHARACTERISTICS OF SAMPLES

1. Mobility and mean free path of graphene

The mobility of graphene was estimated using separate 2D graphene samples without antidot structures. Graphene and h-BN flakes for these samples were exfoliated from the same batch of crystals. Graphene was transferred on h-BN using a reported technique [27–29]. Excepting transfer processes, all the samples were made using the same fabrication process. For 2D graphene samples, dependences of ρ_{xx} on carrier density n are plotted in Fig. 5(a). Apparently the full width at half maximum of the peak structure and values of ρ_{xx} for $|n| > 0.5 \times 10^{12}$ cm^2 are significantly smaller in h-BN graphene than in SiO_2 graphene. This is due to the diminished carrier scattering and potential fluctuation in h-BN graphene. Figure 5(b) shows the carrier density n dependence of mobility. Here, mobility μ_0 was estimated by

$$\mu_0 = 1/[|n|e\rho_{xx}(0)], \tag{A1}$$

where $\rho_{xx}(0)$ is a diagonal resistivity at zero magnetic field. μ_0 for graphene on h-BN reached about 2.1×10^4 cm^2/V s and 3.2×10^4 cm^2/V s at electron and hole densities of 3×10^{12} cm^{-2}, respectively. Both of them increased to about $\sim 7 \times 10^4$ cm^2/V s almost linearly at carrier densities of $\sim 2 \times 10^{11}$ cm^{-2}. In contrast, for graphene on SiO_2, the electron and hole mobilities varied from 1.5×10^4 to 3.7×10^4 cm^2/V s in the same range of carrier density. The mean free path l was estimated using

$$l = \left(\frac{\mu}{e}\right)\hbar k_{\mathrm{F}}, \tag{A2}$$

where $k_{\mathrm{F}} = \sqrt{\pi|n|}$.

2. Determination of number of layers

The layer number of graphene was verified by analyzing the green signal intensity of the digitized optical images. We also used Landau fan diagrams obtained by measuring the V_g and B dependences of the Shubnikov–de Haas effect as shown Figs. 2(a)–2(c). The detailed V_g dependence of R_{xx} and σ_{xy} at high magnetic fields is shown in Figs. 5(c) and 5(d) for antidot samples with $a = 400$ and 200 nm, respectively. Measurements were done at about $B = 7$ T and $T = 4.2$ K. The SdH effect indicated that each Landau level had an identical degeneracy—fourfold—which was verified from the Hall conductivity calculated from $\sigma_{xy} = \rho_{xy}/(\rho_{xx}^2 + \rho_{xy}^2)$, which showed half-integer steps at $\sigma_{xy} = 4e^2(N + 1/2)/h$, $(N = 0, \pm 1, \pm 2, \pm 3, \ldots)$. These facts are hallmarks of single layer graphene.

The V_g dependences of R_{xx} at zero magnetic field are plotted in Figs. 5(e) and 5(f) for monolayer antidot samples with $a = 400$ and 200 nm, respectively.

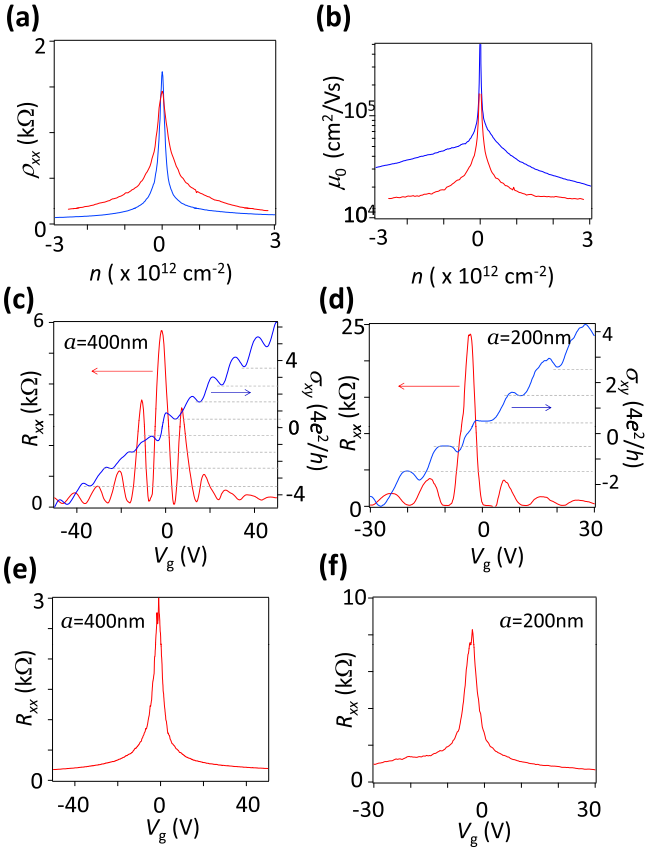

FIG. 5. (Color online) (a) n dependence of ρ_{xx} for a 2D graphene device fabricated to estimate the quality of graphene. (Samples are different from antidot lattices but were made from the same batch of crystal using the same fabrication process.) $T = 4.2$ K. $B = 0$ T. Blue and red curves are for graphene on h-BN and SiO_2 substrate, respectively. (b) n dependence of μ_0 for a 2D graphene device. The blue and red curves are for graphene on h-BN and the SiO_2 substrate, respectively. [The same samples as (a).] (c) V_g dependence of R_{xx} and σ_{xy} for a monolayer antidot device with $a = 400$ nm. $T = 4.2$ K. $B = 7.1$ T. (d) V_g dependence of R_{xx} and σ_{xy} for a monolayer antidot device with $a = 200$ nm. $T = 4.2$ K. $B = 7.5$ T. (e) V_g dependence of R_{xx} of a monolayer antidot sample with $a = 400$ nm. $T = 4.2$ K. $B = 0$ T. (f) V_g dependence of R_{xx} of a monolayer antidot sample with $a = 200$ nm. $T = 4.2$ K. $B = 0$ T.

[1] A. H. Castro Neto, F. Guinea, N. M. R. Peres, K. S. Novoselov, and A. K. Geim, The electronic properties of graphene, Rev. Mod. Phys. **81**, 109 (2009).

[2] A. K. Geim, Graphene: Status and prospects, Science **324**, 1530 (2009).

[3] K. S. Novoselov, A. K. Geim, S. V. Morozov, D. Jiang, M. I. Katsnelson, I. V. Grigorieva, S. V. Dubonos, and A. A. Firsov, Two-dimensional gas of massless dirac Fermions in graphene, Nature (London) **438**, 197 (2005).

[4] D. Weiss, M. L. Roukes, A. Menschig, P. Grambow, K. von Klitzing, and G. Weimann, Electron Pinball and Commensurate Orbits in a Periodic Array of Scatterers, Phys. Rev. Lett. **66**, 2790 (1991).

[5] R. Fleischmann, T. Geisel, and R. Ketzmerick, Magnetoresistance Due to Chaos and Nonlinear Resonances in Lateral Surface Superlattices, Phys. Rev. Lett. **68**, 1367 (1992).

[6] E. M. Baskin, G. M. Gusev, Z. D. Kvon, A. G. Pogosov, and M. V. Entin, Stochastic Dynamics of 2d Electrons in A Periodic Lattice of Antidots, Pis'ma Zh. Eksp. Teor. Fiz. **55**, 649 (1992) [JETP Lett. **55**, 678 (1992)].

[7] S. Ishizaka and T. Ando, Detailed analysis of the commensurability peak in antidot arrays with various periods, Phys. Rev. B **55**, 16331 (1997).

[8] R. Schuster, K. Ensslin, J. P. Kotthaus, M. Holland, and C. Stanley, Selective probing of ballistic electron orbits in rectangular antidot lattices, Phys. Rev. B **47**, 6843 (1993).

[9] R. Schuster, G. Ernst, K. Ensslin, M. Entin, M. Holland, G. W. Böhm, and W. Klein, Experimental characterization of electron trajectories in antidot lattices, Phys. Rev. B **50**, 8090 (1994).

[10] F. Nihey, S. W. Hwang, and K. Nakamura, Observation of large *h/2e* oscillations in semiconductor antidot lattices, Phys. Rev. B **51**, 4649 (1995).

[11] Y. Iye, M. Ueki, A. Endo, and S. Katsumoto, Aharonov-Bohm-type effects in triangular antidot lattice, J. Phys. Soc. Jpn. **73**, 3370 (2004).

[12] D. Weiss, K. Richter, A. Menschig, R. Bergmann, H. Schweizer, K. von Klitzing, and G. Weimann, Quantized Periodic-orbits in Large Antidot Arrays, Phys. Rev. Lett. **70**, 4118 (1993).

[13] F. Nihey and K. Nakamura, Aharonov-Bohm effect in antidot structures, Physica B **184**, 398 (1993).

[14] J. H. Smet, K. von Klitzing, D. Weiss, and W. Wegscheider, dc Transport of Composite Fermions in Weak Periodic Potentials, Phys. Rev. Lett. **80**, 4538 (1998).

[15] F. Nihey, K. Nakamura, T. Takamasu, G. Kido, T. Sakon, and M. Motokawa, Orbital quantization of composite fermions in antidot lattices, Phys. Rev. B **59**, 14872 (1999).

[16] J. Eroms, M. Tolkiehn, D. Weiss, U. Rössler, J. de Boeck, and S. Borghs, Chaotic motion and suppression of commensurability effects in an Andreev antidot billiard, Physica E **12**, 918 (2002).

[17] J. Eroms, D. Weiss, J. De Boeck, G. Borghs, and U. Zülicke, Andreev Reflection at High Magnetic Fields: Evidence for Electron and Hole Transport in Edge States, Phys. Rev. Lett. **95**, 107001 (2005).

[18] C. Albrecht, J. H. Smet, K. von Klitzing, D. Weiss, V. Umansky, and H. Schweizer, Evidence of Hofstadter's Fractal Energy Spectrum in the Quantized Hall Conductance, Phys. Rev. Lett. **86**, 147 (2001).

[19] J. Shabani, M. Shayegan, and R. Winkler, Strain-Induced Fermi Contour Anisotropy of GaAs 2D holes, Phys. Rev. Lett. **100**, 096803 (2008).

[20] J. Eroms and D. Weiss, Weak localization and transport Gap in graphene antidot lattices, New J. Phys. **11**, 095021 (2009).

[21] T. Shen, Y. Q. Wu, M. A. Capano, L. P. Rokhinson, L. W. Engel, and P. D. Ye, Magnetoconductance oscillations in graphene antidot arrays, Appl. Phys. Lett. **93**, 122102 (2008).

[22] R. Yagi, M. Shimomura, F. Tahara, H. Kobara, and S. Fukada, Observing Altshuler-Aronov-Spivak oscillation in a hexagonal antidot array of monolayer graphene, J. Phys. Soc. Jpn. **81**, 063707 (2012).

[23] T. Ando, Exotic electronic and transport properties of graphene, Physica E **40**, 213 (2007).

[24] A. B. Pipard, *Magnetoresistance in Metals* (Cambridge University Press, Cambridge, UK, 1989).

[25] T. J. Thornton, M. L. Roukes, A. Scherer, and B. P. Van de Gaag, Boundary Scattering in Quantum Wires, Phys. Rev. Lett. **63**, 2128 (1989).

[26] S. Masubuchi, K. Iguchi, T. Yamaguchi, M. Onuki, M. Arai, K. Watanabe, T. Taniguchi, and T. Machida, Boundary Scattering in Ballistic Graphene, Phys. Rev. Lett. **109**, 036601 (2012).

[27] C. R. Dean, A. F. Young, I. Meric, C. Lee, L. Wang, S. Sorgenfrei, K. Watanabe, T. Taniguchi, P. Kim, K. L. Shepard, and J. Hone, Boron Nitride Substrates for High-quality Graphene Electronics, Nat. Nanotechnol. **5**, 722 (2010).

[28] T. Taychatanapat, K. Watanabe, T. Taniguchi, and P. Jarillo-Herrero, Quantum Hall Effect And Landau-level Crossing of Dirac Fermions in Trilayer Graphene, Nat. Phys. **7**, 621 (2011).

[29] P. J. Zomer, S. P. Dash, N. Tombros, and B. J. van Wees, A Transfer Technique for High Mobility Graphene Devices on Commercially Available Hexagonal Boron Nitride, Appl. Phys. Lett. **99**, 232104 (2011).